Nanoscale

PAPER

Cite this: *Nanoscale*, 2015, **7**, 15935

Catalyst-free vapour–solid technique for deposition of Bi_2Te_3 and Bi_2Se_3 nanowires/nanobelts with topological insulator properties

J. Andzane,[a] G. Kunakova,[a,b] S. Charpentier,[b] V. Hrkac,[c] L. Kienle,[c] M. Baitimirova,[a] T. Bauch,[b] F. Lombardi[b] and D. Erts*[a]

Received 8th July 2015,
Accepted 28th August 2015

DOI: 10.1039/c5nr04574f

www.rsc.org/nanoscale

We present a simple two-stage vapour–solid synthesis method for the growth of bismuth chalcogenide (Bi_2Te_3, Bi_2Se_3) topological insulator nanowires/nanobelts by using Bi_2Se_3 or Bi_2Te_3 powders as source materials. During the first stage of the synthesis process nanoplateteles, serving as "catalysts" for further nanowire/nanobelt growth, are formed. At a second stage of the synthesis, the introduction of a N_2 flow at 35 Torr pressure in the chamber induces the formation of free standing nanowires/nanobelts. The synthesised nanostructures demonstrate a layered single-crystalline structure and Bi : Se and Bi : Te ratios 40 : 60 at% for both Bi_2Se_3 and Bi_2Te_3 nanowires/nanobelts. The presence of Shubnikov de Haas oscillations in the longitudinal magneto-resistance of the nanowires/nanobelts and their specific angular dependence confirms the existence of 2D topological surface states in the synthesised nanostructures.

Introduction

3D Topological Insulators (TIs) are unconventional bulk insulators that have recently demonstrated remarkable properties, connected to the presence of non-trivial surface metallic states. The surface states exhibit Dirac-like dispersion, where the electron spin is locked perpendicular to the momentum, resulting in the suppression of electron backscattering from nonmagnetic impurities. The unique properties of the topological surface states offer exciting possibilities for use in spintronics[1–5] and quantum information applications,[6–9] as well as for observing exotic phenomena such as Majorana fermions, when brought in proximity with superconductors.[8,10–15] Among the known 3D TIs, bismuth-based compounds, in particular Bi_2Se_3 and Bi_2Te_3, have been widely investigated. They share the same layered rhombohedral crystal structure in the space group D_{3d}^5 ($R\bar{3}m$). In this structure, each charge-neutralized layer is formed by five covalently bonded atomic sheets (for example, Se–Bi–Se–Bi–Se in Bi_2Se_3), defined as a quintuple layer (QL).[16,17] These layers are bonded together by weak (compared to covalent bonds) van der Waals forces to form the crystal. Bi-based TIs have been extensively investigated by angle-resolved photoemission spectroscopy measurements both in single crystals[16,18–20] and in thin films.[21,22] These measurements have shown the two-dimensionality of the surface states with a Fermi surface always shifted of about 300 meV from the Dirac point, anticipating the crucial role of the residual bulk carrier density in the transport properties. Indeed bulk transport can mask the peculiar properties of the surface states, even in samples with low bulk carrier densities.[23] As a consequence, electrical transport experiments aimed at isolating the surface from the bulk contributions remain challenging.[23]

A possible route to detect merely surface effects in 3D topological insulators is to reduce the sample size to the nanoscale, significantly enhancing the surface-to-volume ratio. In fact, 3D TI nanowires are ideal systems to study surface related mesoscopic effects like Aharonov–Bohm interferences, associated with the coherent surface conduction, already observed in Bi_2Se_3 and Bi_2Te_3 nanoribbons[24,25] and nanowires.[26,27] Low dimensional 3D TIs represent also an ideal platform to reveal the Josephson physics of the Majorana modes requiring a reduced number of transport channels.[28,29]

Nanosized bismuth based structures can be synthesized by several methods. For instance, a usual way to fabricate nanocrystalline Bi_2Te_3 is a solution-based chemical process using organic precursors. The drawback of this method is that the residual conduction properties of the synthesized nanocrystalline material are not different from the properties of bulk samples due to the presence of organic residues.[30–33] Regarding nanobelt-like structures, highly crystalline bismuth based nanobelts were fabricated by lithographically patterned galvanic displacement (LPGD) method or by Au-catalysed vapour-

[a]*Institute of Chemical Physics, University of Latvia, LV-1586, Riga, Latvia. E-mail: donats.erts@lu.lv*
[b]*Department of Microtechnology and Nanoscience, Chalmers University of Technology, SE-41296 Göteborg, Sweden*
[c]*Institute of Materials Science, Technical Faculty of the CAU, D-24243 Kiel, Germany*

liquid-solid (VLS) synthesis,[34–37] in some cases followed by AFM-exfoliation to produce ultra-thin topological insulator nanoribbons.[38]

In this work, a method for the synthesis of catalyst-free vapour–solid (VS) highly-crystalline nanoplate-seeded stoichiometric Bi_2Te_3 and Bi_2Se_3 nanowires/nanobelts is described. The nanowires/nanobelts are free standing above the substrate and exhibiting TI properties which have been studied by a complete magneto-electrical characterisation of the synthesised nanowires. The absence of a catalyst insures that the nanostructures are free of contaminants. A thorough analysis of the Shubnikov-de Haas oscillations as a function of the angle between the current and the applied magnetic field and of the temperature enabled us to isolate the signature of the topological surface of the nanowires.

Synthesis process

Catalyst-free vapour–solid (VS) synthesis processes were previously reported for the growth of bismuth selenide and bismuth telluride nanoplates.[17,37,39] However these reports showed that the subsequent growth of the nanobelts on the nanoplate seeds was only possible as a result of catalyst-activated vapour-liquid-solid (VLS) process where Au nanoparticles were used as catalyst. A truly catalyst-free growth of Bi_2Se_3 and Bi_2Te_3 nanostructures includes (i) nanoribbons 1–3 mm long and few hundreds nanometers thick, which were formed during 72 hours in an Ar-filled sealed quartz furnace tube;[40] (ii) Bi_2Se_3 nanostructures (nanowires, nanoribbons, nanoplatelets and nanoflakes) grown using constant Ar/H_2 gas flow;[41] and finally, $BiTe/Bi_2Te_3$ polycrystalline nanowires.[42]

In these reports[41,42] the use of H_2 as carrying gas for the synthesis of Bi_2Se_3 nanostructures has been shown to be of high importance because it binds with Se to form H_2Se, possibly increasing the amount of material transported downstream to the substrate;[41] however, also in H_2 assisted growth the formation of the nanowires and nanoribbons remained a low yield process.

In the case of catalyst-free synthesis of Bi_2Te_3 nanowires[42] chemically synthesised BiTe particles were used as precursors. This method requires complex preliminary synthesis of nanoparticles, followed by their transfer onto the growth substrates. The growth of nanowires from the BiTe nanoparticles seeds resulted in nonstoichiometric Bi_2Te_3. Further annealing of these nanowires in Te rich atmosphere and at high temperature is required to induce phase transformation from BiTe to Bi_2Te_3.[42] It should be mentioned that the annealing of BiTe nanowires in Te rich atmosphere may result in nonhomogeneous transfer of single-crystalline structure of the nanowire to polycrystalline[42] or even to amorphous phase.[43]

Here we present a VS catalyst-free synthesis method for Bi_2Se_3 and Bi_2Te_3 nanowires/nanobelts which is simple and easy to implement. It eliminates the complications of previously reported methods[30–37,40–43] such as contamination with catalyst or organic residues, the use of dangerous gases, complex preliminary preparation of precursor nanoparticles and post-annealing in Te atmosphere to name a few.

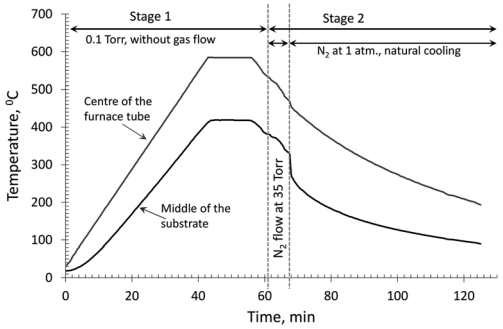

Fig. 1 Time variation of the temperature/pressure/gas flow regime related to the bismuth chalcogenide nanostructures synthesis process.

Before the synthesis, the furnace tube was initially flushed with pure nitrogen for 5 min to remove oxygen residues, pumped down to a base pressure of about 0.1 Torr and sealed. The source material (99.999% Bi_2Te_3 or Bi_2Se_3 powder, Sigma-Aldrich) was placed in the hot centre (so-called "hot zone") of the quartz furnace tube. Microscope glass slides used as substrates for nanostructure deposition were placed 16–20 cm away from the tube centre. The furnace heating and cooling rates were 13 °C min^{-1} and 7–10 °C min^{-1} respectively. During the synthesis, the temperature of the substrate varied between 430 °C at its "hot end" to 230 °C at its "cold end".

The bismuth based nanowires/nanobelts synthesis process consisted of two consequent stages. The 1st stage of the process was aimed at forming bismuth selenide or bismuth telluride nanoplates onto the surface of the substrate. These nanoplates were serving as "catalyst" for the further formation of bismuth selenide or bismuth telluride nanowires/nanobelts. During the 2nd stage of the process, the free-standing nanowires/nanobelts formation on the nanoplates was induced by the inert (N_2) gas flow through the furnace tube. The temperature/pressure/gas flow regime of the synthesis process is illustrated in Fig. 1.

First stage of the synthesis process

During this stage of the growth the centre of the furnace tube was heated up to the temperature of 585 °C at a rate of 13 °C min^{-1} and then held at this temperature for another 15 min and finally cooled down by 50 °C at an average cooling rate of 8 °C min^{-1}. No gas flow was involved during the first synthesis stage. During this stage, the source powder vaporisation occurred, followed by the vapour spread across the whole furnace tube and by the nucleation, on the glass surface irregularities, of the random vaporised material (Fig. 2a and b). The further growth of the nanostructures, from the nucleation centres, occurred during the temperature reduction (Fig. 2c).

After the nucleation, the nanostructure growth continued much faster in lateral dimension than in the vertical dimension and resulted in nanoplate-like structures. The much

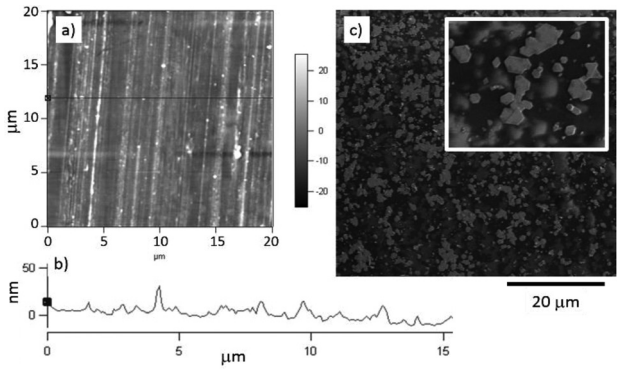

Fig. 2 (a) AFM image and (b) height profile of a glass substrate surface; (c) nanoplate-like bismuth selenide structures (seeds for the following growth of bismuth selenide nanobelts) formed onto the glass surface after the 1st stage of the synthesis process. The inset shows a closer view of the nanoplates.

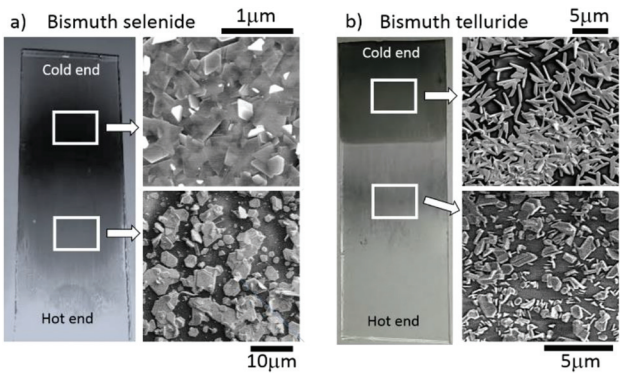

Fig. 3 Photograph (left) and SEM images (right) of bismuth selenide (a) and bismuth telluride (b) nanostructures deposited during the 1st stage of the synthesis process. The shape, density per area unit and chemical composition of these structures depend on the temperature gradient along the substrate.

faster lateral growth of the nanostructures is possibly the result of the layered crystal structure of bismuth chalcogenides in combination with their anisotropic bonding nature.[39] As the top surface of a growing nanoplate is terminated with chemically saturated Te or Se atoms, the atoms further adsorbed from the gas phase could not form covalent bonds with the top Te or Se. Therefore they diffuse around to find the edges of the nuclei where the atoms have dangling bonds ready to form covalent bonds with incoming atoms.[17,36] The temperature gradient along the substrate caused variations in chemical composition and density of the deposited bismuth chalcogenide nanoplates per unit area.

Fig. 3 illustrates the shapes of the deposited bismuth chalcogenide structures *vs.* their location on the substrate surface.

As it is seen from the SEM images (right panels of Fig. 3a and b), the nanostructures deposited closer to the "cold" end of the substrate differ from those deposited closer to the "hot"

Table 1 Data summarising the 1st stage synthesis process, the bismuth chalcogenide nanoplates chemical composition and the location onto the substrate surface

Type of the structure	Temperature increase along the substrate	Bi, %	Se, %	Te, %
Bismuth selenide nanostructures		30 ± 2%	70 ± 2%	—
Bismuth selenide nanoplates		36 ± 3%	64 ± 3%	—
Bismuth selenide nanoplates		38 ± 2%	62 ± 2%	—
Bismuth telluride nanowires/nanowire networks		0.2%	—	99.8%
Bismuth telluride nanoplates		40 ± 2%	—	60 ± 2%
Bismuth telluride nanoplates		50 ± 4%	—	50 ± 4%

end for both bismuth selenide and bismuth telluride. The reason why nanoplate/nanostructure coverage in the cold end is better than the hot end might be related to the temperature of the substrate. The temperature difference between the cold and the hot ends of the substrate is about 200 °C, so the thermally activated surface diffusion coefficient and re-evaporation rates from the substrate are lower in the cold area compared with the hot end. The data regarding the chemical composition of bismuth based nanoplates formed during the 1st stage of the synthesis process are summarised in the Table 1.

The investigation of chemical composition of the deposited bismuth selenide nanostructures shows a change of the Bi : Se ratio from (30 ± 2) : (70 ± 2) at the "cold" areas of the substrate (Fig. 3a top right image) to (38 ± 2) : (62 ± 2) at its "hot" areas (Fig. 3a lower right image). The density of the formed nanoplates per unit area decreases with increasing substrate temperature. For the bismuth telluride, the nanostructures deposited closer to the "cold" end of the substrate are nanowire-networks like (Fig. 3b upper right image). The investigation of their chemical composition shows that these nanowires consist of 99.8% Te with just 0.2% of Bi contamination. The dissociative nature of the evaporation of Bi_2Se_3 and Bi_2Te_3 compounds could be the reason for Te and Se excess in the deposited in the "cold" areas nanostructures as the bond energies of Te–Te and Se–Se are lower than these of Bi–Te and Bi–Se. The structures deposited on the "hotter" areas of the substrate (Fig. 3b lower right image) show an increase of Bi : Te ratio from (40 ± 2) : (60 ± 2) in the middle up to (50 ± 4) : (50 ± 4) at the "hot" end of substrate in correlation with the increase of substrate temperature. The density of formed bismuth telluride nanoplates per surface area unit is almost constant on both ends of the substrate. Both the

bismuth selenide and bismuth telluride nanoplates deposited on the middle and "hot" areas of the substrate exhibit the characteristic bismuth chalcogenides crystalline shapes.[16,17]

Second stage of the synthesis process

The bismuth selenide and bismuth telluride nanowires/nanobelts are synthesised during the 2nd stage of the synthesis process. This stage starts when the centre of the furnace tube is cooled down to 535 °C (see Fig. 1). At that point, the nitrogen gas flow at constant pressure of 35 Torr (which we have found being the optimal pressure for the formation of the bismuth chalcogenide nanowires/nanobelts) is introduced into the furnace tube and kept constant while cooling the centre of the furnace tube in a continuous way down to 475 °C (Fig. 1). Due to the gas flow, the quantity of the source material vapour delivered to the substrate rapidly increased inducing the formation of nanoplate-seeded nanowires/nanobelts. The nanobelts are formed only on those substrate areas where the Bi : Se and Bi : Te ratios of the nanoplates formed during the 1st stage of the synthesis process is close to *ca.* 40 : 60 at%, representing the stoichiometry of perfect bismuth selenide (Bi_2Se_3) and bismuth telluride (Bi_2Te_3). It is not excluded that the nanowire/nanobelt like structures would probably grow from the non-stoichiometric "seeds" under different experimental conditions (temperature and pressure regime). However in this work we have concentrated on the growth of stoichiometric Bi2Se3/Bi2Te3 nanostructures. Nanobelts/nanowires formation always starts on the faces/surface of the pre-formed nanoplates. Examples of the synthesised bismuth telluride and bismuth selenide nanobelts are shown in Fig. 4.

The nanowires/nanobelts reach lengths up to 50 μm and widths between 20 and 800 nm. The amount of the fabricated nanostructures calculated from the SEM images is approx. (1–5) × 10^6 nanobelts/nanowires per mm^2 for bismuth selenide (Fig. 4a and b) and (1–5) × 10^4 nanobelts/nanowires per mm^2 for bismuth telluride (Fig. 4c) which is relatively high in comparison with other reported catalyst-free synthesis methods.[40–42] The growth process was terminated and the synthesis process was completed by filling the furnace tube with gaseous nitrogen until 1 atm pressure was achieved and then cooling down to room temperature. The synthesised nanowires/nanobelts are free standing above the substrate in contradiction to the nanoplates, which are strongly bonded to the substrate. Thus, they can be easily transferred from the growth substrates onto the pre-patterned substrates (Si/SiO_2, Si/46 nm AlO) for electrical measurements or TEM grids by using adhesive tape or direct mechanical contact between the growth and characterisation substrates.

Characterisation of synthesised nanowires/nanobelts

Structural and chemical investigations. The thickness and smoothness of the surfaces of the synthesised bismuth selenide and bismuth telluride nanowires/nanobelts were measured by AFM (Fig. 5).

The thicknesses of the nanowires/nanobelts ranged from 20 up to 100 nm. They often present a step-like structure (Fig. 5b) with height variations of discreet 1, 2 or 3 nm (Fig. 5b) corresponding to single, double or triple quintuple layer difference. The roughness of the top layer of the nanobelt surface does not exceed ±0.2 nm (Fig. 5c, inset).

Structural and chemical investigations of synthesised nanobelts/nanowires were performed by HRTEM and are presented in the Fig. 6.

The morphology of bismuth telluride and bismuth selenide nanostructures is depicted in the bright field images of Fig. 6a (left and right images respectively). For all the investigated samples we find stripes of dark contrast propagating throughout the nanobelt, which appear due to bending of the nanostructure.[44] Further, for some bismuth telluride nanobelts

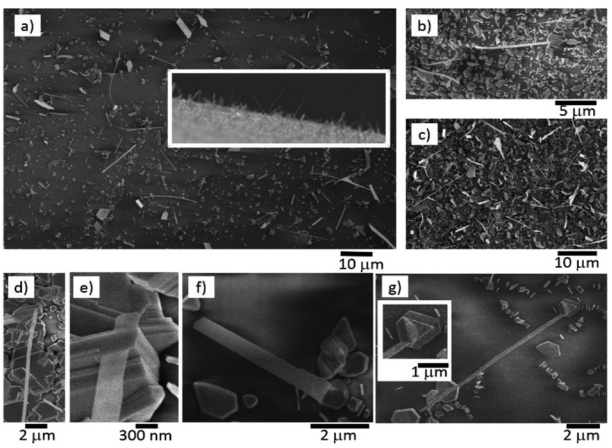

Fig. 4 SEM images of bismuth selenide (a) – top view, (b) – side view of the nanowires/nanobelts which are free-standing above the substrate surface (d–f) – closer view of the separate nanobelts) and bismuth telluride nanobelts (c) – top view, (g) – closer view of separate nanobelt) synthesised during the 2nd stage of the synthesis process. Nanobelts are nanoplate-seeded and free-standing above the substrate surface; (g-inset), (e) closer view of the nanobelt seeds.

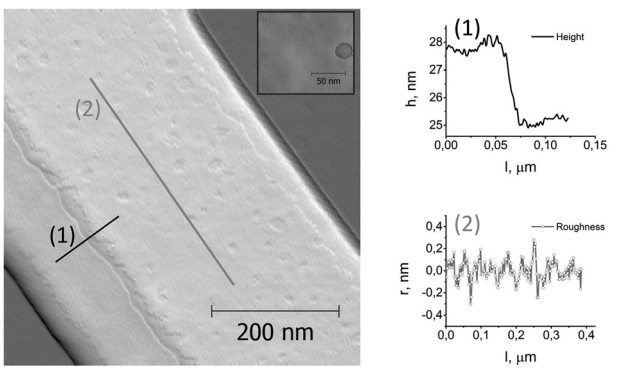

Fig. 5 (a) AFM image of a bismuth chalcogenide nanobelt. The inset shows a closer view of the top layer of the nanobelt surface illustrating the presence of hole-like irregularities (height variation approx. 0.5 nm); (b) height profiles illustrating step-like structure of the nanobelt; (c) height profile illustrating surface roughness of the nanobelt (the height variations do not exceed ±0.2 nm).

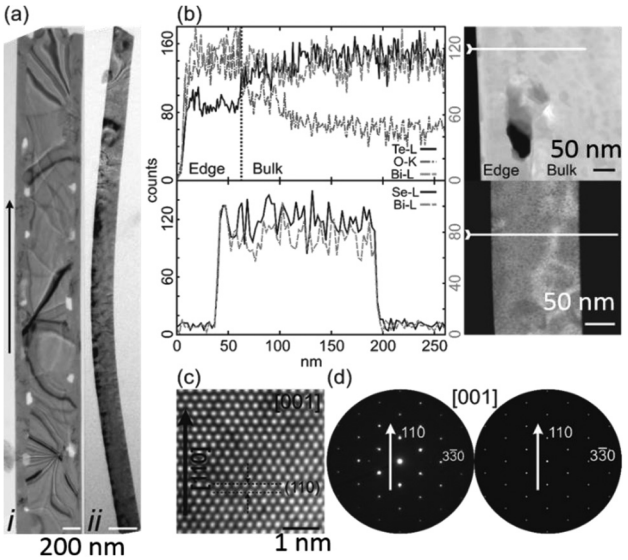

Fig. 6 TEM investigations on bismuth chalcogenide nanobelts. The arrows mark the growing direction along the [110] direction. (a) Bright field images of a bismuth telluride (a-i) and bismuth selenide (a-ii) images. (b) STEM-EDX nanoprobe analyses with corresponding STEM images (left): (top) bismuth telluride nanobelt, from the marked area in the STEM image (right). Te and O share the left *y*-axis, Bi the right *y*-axis. The dashed black line marks the boundary between two chemically different areas (edge, bulk); (bottom) bismuth selenide nanobelt (c) HRTEM micrograph recorded with an objective lens defocus of *ca.* −20 nm. (d) Electron diffraction studies along the [001] zone axis with the experimental data (left) *vs.* calculated simulation based on the $R\bar{3}m$ symmetry. The data of (c) and (d) are taken from bismuth telluride and are analogues to the findings of bismuth selenide.

(Fig. 6a (left image)) holes were detected near the longitudinal edges. Chemical analysis of the bismuth telluride nanobelts revealed the presence of two distinct regions, separating into an edge and a bulk area (Fig. 6b (top)). The width of the respective areas was determined to be *ca.* 80 nm (edge) and 580 nm (bulk). For the bulk area the median of the Te–Bi ratio was calculated to be *ca.* 60 : 40 at% using STEM-EDX nanoprobe point measurements. Applying the same experimental methods for the edge area, a higher Bi content along with considerable oxidisation was detected (Fig. 6b (top)). The holes are always located at the border between these two areas, as visible in the STEM image of Fig. 6b (right top). As possible interpretation, the oxide layer at the edge of the nanobelt induces additional strain fields at the interface regions, causing the formation of the holes.[44–46]

The analysis of the bismuth selenide nanobelt did not show impurities and significant variations in chemical composition across it (Fig. 6b (bottom)). For the bismuth selenide nanobelt the calculated median of the Se–Bi ratio was 60 : 40 at %. The bulk area of the bismuth telluride nanobelt and the middle area of the bismuth selenide nanobelt demonstrate a single crystalline behaviour, as depicted by the high resolution studies in Fig. 6c. Assuming the space group $R\bar{3}m$ the zone axis can be assigned to [001]. The growing direction is perpendicular to the (110) planes and, therefore, must be along [110], as marked in the associated HRTEM micrograph and FFT pattern of the Fig. 6d. These findings were verified on a larger scale by applying SAED. The edge area of the bismuth telluride nanobelt is also crystalline; however, high resolution investigations exhibited a high density of defects. The Moiré patterns were observed in HR TEM image and in corresponding SAED image (Fig. 6c and d) indicating a superlattice structure that could be related to the bismuth excess in that region.[36]

The nanowire/nanobelt formation and their growth direction could have this simple explanation. The crystal structure of stoichiometric Bi_2Se_3 and Bi_2Te_3 has a layered hexagonal (honeycomb) architecture where Bi planes alternates with Se/Te planes. For a honeycomb structure, there are six equivalent vertex directions. When there is no temperature gradient, the nanostructure grows uniformly in all in plane directions of the substrate resulting in a [001] growth. This is also favourite by the lower surface energy of this orientation (compared to others) with the specific substrate used in this work.[48] This results in the formation of nanoplatelets [001] oriented with the Bi and Se/Te planes parallel to the surface of the substrate. As it is mentioned above, the growth of the nanoplatelets continues much faster in lateral dimension than in the thickness [001] dimension due to the layered crystal structure of bismuth selenide/telluride, in combination with anisotropic bonding nature and high surface diffusion rate of the adsorbed on the top surface atoms. Without the temperature gradient, such growth will rather result in formation of nanostructured thin film, not in formation of the nanowires growing in [001] direction. In presence of a temperature gradient, which is the result of the gas flow introduction into the furnace tube along its axis when the temperature in its centre is 535 °C, the 6-fold symmetry of the vertex directions can be broken, and the nanowires/nanobelts can grow along this gradient direction (Fig. 4d–g). In the case of the nanowires/nanobelts we have investigated by HRTEM, this direction is the [110] one, which corresponds to one of the vertex direction of a hexagon and matches the direction of the temperature gradient. The fact that the [110] growth happens on top of the nanoplatelets, instead of the bare substrate, we believe might be due to the lower surface energy for an homoepitaxial growth (even though with a different orientation of the nanoplatelets) compared to the growth on the substrate. As the nanowire/nanobelt grows along [110] direction, with the (001) facets as top and bottom surfaces and (110) facets as side surfaces, it has rectangular cross section.[37]

Resistance *versus* temperature measurements

The resistance *versus* temperature dependence of the nanowire/nanobelt was obtained using a four point measurement setup in the range 2–300 K. To achieve low contact resistances the surface of the nanowire/nanobelt was cleaned with a gentle Ar^+ ion milling before the deposition of the bilayer Ti/Au. An AFM image of a single nanowire/nanobelt device for a 4-point electrical characterisation is shown in Fig. 7a. The

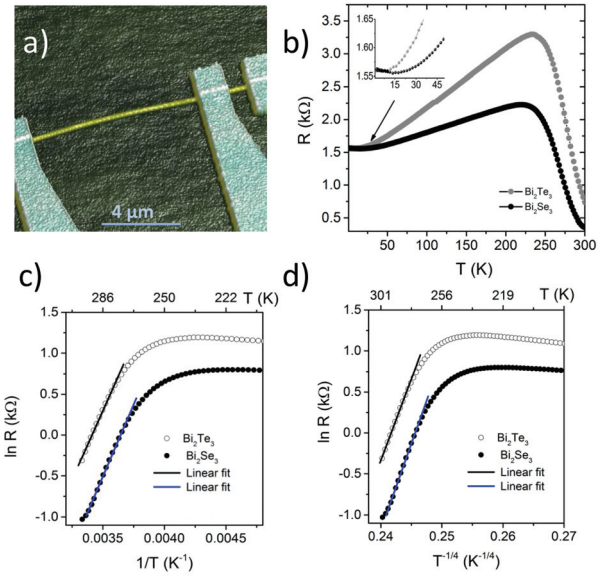

Fig. 7 (a) AFM image of a Bi_2Se_3 nanowire/nanobelt contacted with 4 electrodes (only three are visible) (b) resistance of the bismuth telluride and bismuth selenide nanowires/nanobelts *versus* temperature; (c) and (d) ln(R) as a function of the $1/T$ and $T^{-1/4}$ with linear fits corresponding to the activation and variable range hopping conduction.

resistance *versus* temperature measurements of both Bi_2Se_3 and Bi_2Te_3 nanowires/nanobelts are shown in Fig. 7b.

For all measured samples a broad hump of the resistance was observed in the temperature range from 150–250 K. At lower temperatures 2–15 K the resistance, instead, remained practically constant. A similar behaviour was previously reported for both patterned Bi_2Se_3 thin films and individual nanowires[27,47] and it has been attributed to the specifics of the carriers from the bulk and the surface in TIs. The broad hump can indeed be explained by the presence of two types of carriers originating from the surface and the bulk. By lowering the temperature, the concentration of the bulk charge carriers becomes supressed and the surface carriers dominate the conduction.[25] The activation energy E_A for the bulk carriers can be determined by the relation $R \sim e^{E_A/k_BT}$. Plotting the ln(R) as a function of $1/T$ (Fig. 7c), we have determined the values of the activation energies, from the linear slope at high temperatures, as 0.31 and 0.22 eV for Bi_2Se_3 and Bi_2Te_3 respectively. These values are comparable with the bandgap energies for the crystals.[18,49]

However, the resistance in the high temperature region is also found to follow the 3D variable hopping range conduction (VRH) as $R \sim e^{(T/T_o)-1/4}$ where T_o is a constant (Fig. 7d).[50] The observation of the VRH conduction is also typical of bulk insulator and it has already been found in doped Bi-based compounds.[22,51] In our nanowires, we cannot discriminate between the two mechanisms; however whatever scenario is realised in the nanostructures the resistance *vs.* temperature at high temperature is typical of an insulator while at low temperature the transport becomes the parallel of the insulating component and a metallic component (resulting in a decreasing resistance with decreasing temperature) that nearly saturates below 20 K (see Fig. 7b). For Bi_2Se_3 nanowires/nanobelts (Fig. 7b, inset) below 15 K a weak upturn is observed which might be addressed to electron–electron interactions.[27]

Shubnikov de Haas oscillations of the Bi_2Se_3 nanowires/nanobelts

To prove the existence of the topologically protected surface states the longitudinal and transversal magnetoresistance R_{xx} and R_{xy} respectively of the nanowires/nanobelts were measured in presence of a magnetic field, perpendicular to the nanowire/nanobelt, up to 14 T. To achieve low contact resistances the surface of the nanowire was cleaned with a gentle Ar^+ ion milling before the deposition of the bilayer Ti/Au.[52] The Hall effect measurements of the individual TI nanowire/nanobelt will be discussed in the separate report. Here we will focus on the observation of pronounced resistance R_{xx} modulation (Fig. 8a) that we demonstrate can be ascribed to the Shubnikov-de Haas (SdH) oscillations typical of a two dimensional electron gas.[53,54]

It is important to point out that for all the nanowires/nanobelts the measured longitudinal resistance $R_{xx} \gg R_{xy}$, which leads to $G_{xx} \approx 1/R_{xx}$. This conditions allows to construct the Fan diagram by indexing the maxima of R_{xx}.[23] Fig. 8c shows the Fan diagram were the Landau level indexes (N), determined from the maxima of R_{xx}, are plotted as a function of their position in the inverse field $1/B_n$:[23]

$$(2N-1) = 2\left(\frac{F}{B_n} - \frac{1}{2} + \beta\right) \quad (1)$$

Here B_n is the normal component of the field, F is the frequency and β is the phase factor of the SdH oscillations. From the fitting of the linear slope of the fan diagram we obtain the frequency of the oscillations, F = 96 T. This value is also in agreement with the one obtained by considering a fast Fourier transform (FFT) of the data, as shown in the inset of Fig. 8c. Using the frequency of the oscillations and the Onsager's relation:[23]

$$F = \left(\frac{\hbar c}{2\pi e}\right) 2\pi k_F^{\,2} = \left(\frac{\hbar c}{2\pi e}\right) 2\pi n_{2D} \quad (2)$$

we have extracted the two dimensional carrier density n_{2D} = 2.3 × 10^{12} cm^{-2} and the Fermi wave vector k_F = 0.054 $Å^{-1}$ at 2 K. The extracted values, for the various nanowires/nanobelts, are listed in the Table 2.

The intercept from the Landau level fan diagram, β = 0.56, is in excellent agreement with the value β = 0.5, expected for Dirac electrons, which possess a Berry phase $\phi_B = 2\pi\beta = \pi$.[23] The occurrence of an intercept close to 0.5 has been verified for all the nanowires/nanobelts shown in Fig. 8a, which strongly indicates that the SdH oscillations are coming from the topological surface states.

A further proof of the origin of the SdH oscillations, can be provided by a study of the behavior of F as a function of the

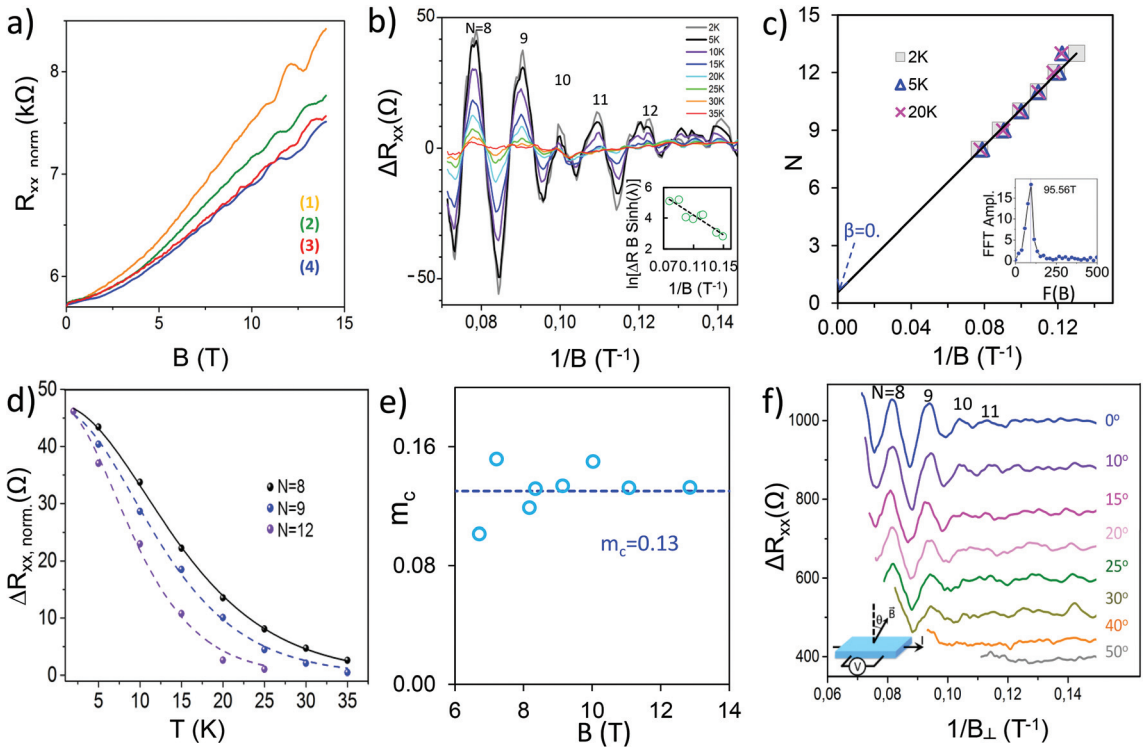

Fig. 8 (a) Magnetoresistance of the Bi_2Se_3 nanowires/nanobelts at T = 2 K: the different curves refer to different nanowires/nanobelts. The data are normalised to the curve (2) using the value at B = 0 T; (b) Shubnikov-de Haas oscillations of the Bi_2Se_3 nanowire/nanobelt (2) of (a) measured at different temperatures (2–35 K). The inset shows the Dingle plot at T = 2 K, the dashed line corresponds to the linear fit; (c) Fan diagram of the oscillations presented in (b), where the Landau level indexes are plotted as a function of 1/B. Inset: FFT analysis of the SdH oscillations at 2 K; (d) amplitude ΔR_{xx} of the SdH oscillations *versus* temperature, the solid and dashed lines corresponds to the fit of eqn (3) used to determine the cyclotron frequency. The data are normalised to the curve N = 8 using the value at T = 2 K; (e) the extracted cyclotron mass m_c as a function of the magnetic field. The horizontal line represents the value obtained from the ARPES data for single Bi_2Se_3 crystal [54], 0.13m_e; (f) Shubnikov-de Haas oscillations, after the subtraction of the smooth background, plotted *versus* $1/B\perp \equiv 1/(B\cos\theta)$, where the θ is the angle between magnetic field and the plane of the nanowire/nanobelt. The curves are shifted along the y axis.

Table 2 Calculated parameters of the Bi_2Se_3 nanowires/nanobelts and comparison with literature data. ρ – resistivity at zero field and T = 2 K, β – intercept from the Landau level fan diagram, n_{2D} – two dimensional carrier density, m_c – cyclotron mass, F – frequency of the SdH oscillations, k_F – Fermi wave vector, v_F – Fermi velocity, E_F – position of the Fermi level, τ – surface lifetime, μ_s – mobility. * The value of the cyclotron mass indicated with * has been used to calculate the physical parameters for the nanowires/nanobelts (3) and (4). Ref. 54 indicated with double asterisks ** has been used to get an estimate of the physical parameters of Bi_2Se_3 single crystal

NR	ρ (Ω cm)	β	n_{2D} (cm^{-2})	m_c ($\times m_e$)	F (T)	k_F (A^{-1})	v_F ($\times 10^5$ m s^{-1})	E_F (eV)	τ ($\times 10^{-13}$ s)	μ_s (cm^2 V^{-1} s^{-1})
1		0.54	2.48×10^{12}	0.139	102.2	0.056	4.85	0.177	2.1	2820
2		0.56	2.31×10^{12}	0.133*	95.5	0.054	4.69	0.166	4.7	6184
3	5.2×10^{-4}	0.81	2.22×10^{12}	—	91.4	0.053	4.59	0.16	5.5	7311
4	3.8×10^{-4}	0.46	1.49×10^{12}	—	61.4	0.043	3.76	0.107	6.2	8225
Ref. 40	2.4×10^{-4}	0.50	3.16×10^{12}	0.18	131	0.063	3.96	0.176	4	3926
Ref. 53		0.81	1.30×10^{12}	0.117						1200
Ref. 54**	~2.3–11 $\times 10^{-4}$			0.13 (ARPES)						

angle θ between the magnetic field and the surface of the sample. Specifically, in the case of a 2D transport, F changes as 1/cosθ, while a 3D system shows deviations from this dependence, in particular at high angles.[13,23,53] Plotting the oscillatory part of the longitudinal resistance as a function of $1/(B\cos\theta)$ (see Fig. 8f) one can expect the oscillations at various angles to align if the system is 2D, as shown in Fig. 8f. This confirms that the oscillations originate from the 2D surface states. It is worth mentioning that in many recent reports, on the topological properties of surface states of TIs, the measurement of the angular dependence of the SdH oscillations is missing which makes the attribution of the oscillation to the existence of two dimensional surface states rather questionable.

The temperature dependence of the SdH oscillations has been measured in the range of temperature 2 to 35 K (Fig. 8b). The decay of the amplitude of the oscillations ΔR_{xx} by increasing the temperature is shown in Fig. 8d and it can be used to extract the cyclotron frequency ω_c and the mass m_c. For a given magnetic field:[53]

$$\Delta R_{xx} \propto \frac{2\pi^2 k_B T/\hbar\omega_c}{\sinh(2\pi^2 k_B T/\hbar\omega_c)} \quad (3)$$

where k_B is the Boltzmann constant and $\hbar$ is the Planck's constant. From the fitting of ΔR_{xx} as a function of T using the expression (3) to extract ω_c one obtains the cyclotron mass using the relation $m_c = qB/\omega_c$. We have extracted the value for ω_c for different peaks at different magnetic fields and we have consistently obtained values $m_c = 0.133m_e$, where m_e is the free electron mass (Fig. 8e). The value for m_c corresponds well with previous ARPES and SdH measurements for Bi_2Se_3 single crystal and nanoribbons.[40,53,54]

Using the cyclotron mass, the Fermi velocity v_F can be derived from the relation $v_F = \hbar k_F/m_c$; knowing v_F the position of the Fermi level E_F can be obtained from the relation $E_F = m_c v_F^2$.

The extracted values for $v_F = 4.7 \times 10^5$ m s^{-1} and $E_F = 166$ meV are in agreement with other reports for Bi_2Se_3 nanoribbons (Table 2).[40]

To evaluate the mobility of the surface states we estimate the quantum lifetime from the slope of the Dingle plot (Fig. 8b, inset) expressed by the relation:

$$\mathrm{In}[\Delta R_{xx} B \sinh(\lambda(T))] \approx 1/B \times [2\pi^2 E_F/\tau e v_F^2] \quad (4)$$

where $\lambda(T) = 2\pi^2 k_B T m_c/\hbar e B$[25] is the thermal factor The extracted surface lifetime τ is in order of 4.7×10^{-13} s. This allows us to calculate the mean free path $l = v_F\tau = 219$ nm and surface mobility $\mu_s = e\tau/m_c = 6184$ cm^2 V^{-1} s^{-1} at base temperature $T = 2$ K. This value, as well as the other values we have obtained for other devices (reported in Table 2) are higher than the ones previously reported for Bi_2Se_3 ribbons[40,53] confirming the very high quality of our nanowires/nanobelts and the validity of our approach to growth TI nanostructures beyond the present state of art.

Table 2 collects the various parameters extracted from the SdH oscillations related to the different measured devices.

Summary and conclusions

We have presented a synthesis method for catalyst-free vapour–solid deposition of bismuth selenide and bismuth telluride nanowires/nanobelts using Bi_2Se_3 and Bi_2Te_3 powders as source materials.

The synthesis process consists of two stages of growth: during the 1st stage, which occurs without any gas flow under low pressure through the furnace tube, the nanoplates (serving as "catalyst" for the growth of the nanowires/nanobelts) are formed from the source material; during the 2nd stage, the nanowires/nanobelts are grown starting from the previously formed nanoplates. The formation of the nanowires/nanobelts occurs under a lower temperature compared with the 1st stage temperatures and is initiated by the gas flow introduced into the furnace tube for a short period of time. The synthesised nanobelts are free-standing above the substrate surface which facilitates their transfer to another substrates.

The advantages of the developed method are its simplicity (no preliminary preparation of precursor nanoparticles is required), the applicability for both Bi_2Te_3 and Bi_2Se_3 nanowire/nanobelt synthesis, rapid growth times, exclusion of H_2 gas from the synthesis process, as well as the absence of contamination of deposited structures with catalyst residues. With our approach we get stoichiometric Bi_2Te_3, without the necessity to use a post-annealing of the synthesised nanostructures in Te rich atmosphere as in other reports.[42,43] This simplifies the synthesis process and excludes the risk of phase transformation in the nanowires/nanobelts. The synthesis presented in this work is highly reproducible and results in single-crystalline stoichiometric Bi_2Se_3 and Bi_2Te_3 (confirmed by EDX). The relative high yield production – approx. (1–5) × 10^6 nanowires/nanobelts per mm^2 for bismuth selenide and (1–5) × 10^4 nanowires/nanobelts per mm^2 for bismuth telluride and the high level of reproducibility of the synthesised nanowires/nanobelts are also of significant relevance.

We have investigated the nanostructures using HRTEM, SAED and AFM. Both the Bi_2Se_3 and Bi_2Te_3 compositions demonstrate a layered structure and single-crystalline behaviour and are sharing the same $R\bar{3}m$ space group.

We have presented a complete electrical characterisation of the topological surface layer of Bi_2Se_3 nanowires/nanobelts. Our results show a high degree of reproducibility between the different nanostructures. Through the analysis of the angular dependence and position of the maxima of the Shubnikov-de Haas oscillations, we confirmed that they originate from the presence of the 2D topological surface states characterised by Dirac electron. Moreover we extract among the highest values for the mobility of the two dimensional topological surface states of about 8000 cm^2 V^{-1} s^{-1}.

These results are also an important step towards the detection of Majorana fermions physics. Indeed the decrease of the number of channels in Josephson devices, by squeezing the dimensions of 3D topological insulators is a mandatory requirement for the observation of Marojana fermions phenomenology.[14,15]

Experimental

The synthesis process was carried out in a horizontal 53 cm tube of a single-zone quartz tube furnace (GSL-1100X, MTI Corp.) The morphology and chemical composition of growth products were analysed using a field emission scanning electron microscope Hitachi S-4800 equipped with a Bruker XFlash Detector 5010 for Energy Dispersive X-ray Spectrometry (EDS) measurements. The thicknesses and surface morphology of the nanowires/nanobelts were determined by an atomic

force microscope Asylum Research MFP-D. The structural analysis was performed by using a FEI Tecnai F30 G^2 STwin operated at 300 kV, applied with a field emission gun (FEG). The spherical aberration coefficient was C_S = 1.2 mm. Selected Area Electron Diffraction (SAED) patterns were recorded using an aperture, which limited the diffraction to an area of 250 nm. All High Resolution (HR) Transmission Electron Microscopy (TEM) and ED pattern were evaluated with the analysis software Digital Micrograph 3.6.1 (Gatan, Inc.) (DM). For the contrast enhancement of HRTEM the filter plug-in for DM was applied.[55] Simulations of SAED patterns were calculated using the JEMS program package.[56] Metal electrodes (5 nm Ti/95 nm Au) for current–voltage measurements were fabricated across the nanowires/nanobelts using Ar ion etching (Oxford Ionfab 300 Ion Beam System) and electron beam lithography techniques (JEOL JBX-300FS). Magnetoresistance and temperature dependence measurements were performed in a Physical Property Measurement System (PPMS Quantum Design).

Acknowledgements

This work is supported by the Latvia National Research Program IMIS 2, the Swedish Research Council (VR) the Swedish Foundation for Strategic Research (SSF) under the project "Graphene based high-frequency electronics" and by the KAW foundation under the project "Dirac Materials". Clean-room processing has been achieved using equipment sponsored by the Knut and Alice Wallenberg Foundation.

Notes and references

1 D. Pesin and A. H. MacDonald, *Nat. Mater.*, 2012, **11**, 409.
2 Y. Shiomi, K. Nomura, Y. Kajiwara, K. Eto, M. Novak, K. Segawa, Y. Ando and E. Saitoh, *Phys. Rev. Lett.*, 2014, **113**, 196601.
3 J. Tian, I. Childres, H. Cao, T. Shen, I. Miotkowski and Y. P. Chen, *Solid State Commun.*, 2014, **191**, 1.
4 C. H. Li, O. M. van't Erve, J. T. Robinson, Y. Liu, L. Li and B. T. Jonker, *Nat. Nanotechnol.*, 2014, **9**, 218.
5 A. R. Mellnik, J. S. Lee, A. Richardella, J. L. Grab, P. J. Mintun, M. H. Fischer, A. Vaezi, A. Manchon, E.-A. Kim, N. Samarth and D. C. Ralph, *Nature*, 2014, **511**, 449.
6 C. Nayak, S. H. Simon, A. Stern, M. Freedman and S. D. Sarma, *Rev. Mod. Phys.*, 2008, **80**, 1083.
7 J. Moore, *Nat. Phys.*, 2009, **5**, 378.
8 M. Z. Hasan and C. L. Kane, *Rev. Mod. Phys.*, 2011, **82**, 3045.
9 A. Stern, *Nature*, 2010, **464**, 187.
10 J. Nilsson, A. R. Akhmerov and C. W. J. Beenakker, *Phys. Rev. Lett.*, 2008, **101**, 120403.
11 L. Fu and C. L. Kane, *Phys. Rev. Lett.*, 2008, **100**, 096407.
12 Y. Tanaka, T. Yokoyama and N. Nagaosa, *Phys. Rev. Lett.*, 2009, **103**, 107002.
13 L. Galletti, S. Charpentier, M. Iavarone, P. Lucignano, D. Massarotti, R. Arpaia, Y. Suzuki, K. Kadowaki, T. Bauch, A. Tagliacozzo, F. Tafuri and F. Lombardi, *Phys. Rev. B: Condens. Matter*, 2014, **89**, 134512.
14 M. Veldhorst, M. Snelder, M. Hoek, T. Gang, V. K. Guduru, X. L. Wang, U. Zeitler, W. G. van der Wiel, A. A. Golubov, H. Hilgenkamp and A. Brinkman, *Nat. Mater.*, 2012, **11**, 417.
15 M. Veldhorst, C. G. Molenaar, X. L. Wang, H. Hilgenkamp and A. Brinkman, *Appl. Phys. Lett.*, 2012, **100**, 072602.
16 H. J. Zhang, X. C. Liu, X. L. Qi, X. Dai, Z. Fang and S. C. Zhang, *Nat. Phys.*, 2009, **5**, 438.
17 D. Kong, W. Dang, J. J. Cha, H. Li, S. Meister, H. Peng, Z. Liu and Y. Cui, *Nano Lett.*, 2010, **10**, 2245.
18 Y. Xia, D. Qian, D. Hsieh, L. Wray, A. Pal, H. Lin, A. Bansil, D. Grauer, Y. S. Hor, R. J. Cava and M. Z. Hasan, *Nat. Phys.*, 2009, **5**, 398.
19 Y. L. Chen, J. G. Analytis, J.-H. Chu, Z. K. Liu, S.-K. Mo, X. L. Qi, H. J. Zhang, D. H. Lu, X. Dai, Z. Fang, S. C. Zhang, I. R. Fisher, Z. Hussain and Z.-X. Shen, *Science*, 2009, **325**, 178.
20 D. Hsieh, Y. Xia, D. Qian, L. Wray, J. H. Dil, F. Meier, J. Osterwalder, L. Patthey, J. G. Checkelsky, N. P. Ong, A. V. Fedorov, H. Lin, A. Bansil, D. Grauer, Y. S. Hor, R. J. Cava and M. Z. Hasan, *Nature*, 2009, **460**, 1101.
21 J. J. Lee, F. T. Schmitt, R. G. Moore, I. M. Vishik, Y. Ma and Z. X. Shen, *Appl. Phys. Lett.*, 2012, **101**, 013118.
22 Y. Y. Li, G. Wang, X. G. Zhu, M. H. Liu, C. Ye, X. Chen, Y. Y. Wang, K. He, L. L. Wang, X. C. Ma, H. J. Zhang, X. Dai, Z. Fang, X. C. Xie, Y. Liu, X. L. Qi, J. F. Jia, S. C. Zhang and Q. K. Xue, *Adv. Mater.*, 2010, **22**, 4002.
23 Y. Ando, *J. Phys. Soc. Jpn.*, 2013, **82**, 102001, arXiv:1304.5693v2.
24 H. Peng, K. Lai, D. Kong, S. Meister, Y. Chen, X.-L. Qi, S.-C. Zhang, Z.-X. Shen and Y. Cui, *Nat. Mater.*, 2010, **9**, 225.
25 F. Xiu, L. He, Y. Wang, L. Cheng, L.-T. Chang, M. Lang, G. Huang, X. Kou, Y. Zhou, X. Jiang, Z. Chen, J. Zou, A. Shailos and K. L. Wang, *Nat. Nanotechnol.*, 2011, **6**, 216.
26 B. Hamdou, J. Gooth, A. Dorn, E. Pippel and K. Nielsch, *Appl. Phys. Lett.*, 2013, **103**, 193107.
27 M. Tian, W. Ning, Z. Qu, H. Du, J. Wang and Y. Zhang, *Sci. Rep.*, 2013, **3**, 1212.
28 A. C. Potter and L. Fu, *Phys. Rev. B: Condens. Matter*, 2013, **88**, 121109(R).
29 M. Snelder, M. Veldhorst, A. A. Golubov and A. Brinkman, *Phys. Rev. B: Condens. Matter*, 2013, **87**, 104507.
30 A. Purkayastna, S. Kim, D. D. Gandhi, P. G. Ganesan, T. Borca-Tasciuc and G. Ramanath, *Adv. Mater.*, 2006, **18**, 2958.
31 M. R. Dirmyer, J. Martin, G. S. Nolas, A. Sen and J. V. Badding, *Small*, 2009, **5**, 933.
32 M. Scheele, N. Oeschler, K. Meier, A. Kornowski, C. Klinke and H. Weller, *Adv. Funct. Mater.*, 2009, **19**, 3476.
33 M. E. Anderson, S. S. N. Bharadway and R. E. Schaak, *J. Mater. Chem.*, 2010, **20**, 8362.

34 H. Jung, Y. Rheem, N. Chartuprayoon, J.-H. Lim, K.-H. Lee, B. Yoo, K. Lee, Y.-H. Choa, P. Wei, J. Shi and N. V. Myung, *J. Mater. Chem.*, 2010, **20**, 9982.

35 Q. Wei, Y. Su, C. J. Yang, Z. G. Liu, H. N. Xu, Y. D. Xia and J. Yin, *J. Mater. Sci.*, 2011, **46**, 2267.

36 B. Hamdou, J. Kimling, A. Dorn, E. Pippel, R. Rostek, P. Woias and K. Nielsch, *Adv. Mater.*, 2013, **25**, 239.

37 D. Kong, J. C. Randel, H. Peng, J. J. Cha, S. Meister, K. Lai, Y. Chen, Z.-X. Shen, H. C. Manoharan and Y. Cui, *Nano Lett.*, 2010, **10**, 329.

38 S. S. Hong, W. Kundhikanjana, J. J. Cha, K. Lai, D. Kong, S. Meister, M. A. Kelly, Z.-X. Shen and Y. Cui, *Nano Lett.*, 2010, **10**, 3118.

39 S. Wi, E. Elezi, A. C. Liu, V. Ray, K. Sun and X. Liang, *Appl. Phys. A*, 2013, **111**, 755.

40 L. Fang, Y. Jia, D. J. Miller, M. L. Latimer, Z. L. Xiao, U. Welp, G. W. Crabtree and W.-K. Kwok, *Nano Lett.*, 2012, **12**, 6164.

41 J. T. Mlack, A. Rahman, G. L. Johns, K. J. T. Livi and N. Markovic, *Appl. Phys. Lett.*, 2013, **102**, 193108.

42 C.-L. Hsin, M. Wingert, C.-W. Huang, H. Guo, T.-J. Shin, J. Suh, K. Wang, J. Wu, W.-W. Wu and R. Chen, *Nanoscale*, 2013, **5**, 4669.

43 B. Hamdou, J. Kimling, A. Dorn, E. Pippel, R. Rostek, P. Woias and K. Nielsch, *Adv. Mater.*, 2013, **25**, 239.

44 Y. Ding and Z. L. Wang, *J. Phys. Chem. B*, 2004, **108**, 12280.

45 R. Adelung, O. A. Aktas, J. Franc, A. Biswas, R. Kunz, M. Elbarhi, J. Kanzow, U. Schürmann and F. Faupel, *Nat. Mater.*, 2004, **3**, 375.

46 M. Elbahri, S. K. Rudra, S. Wille, S. Jebril, M. Scharnberg, D. Paretkar, R. Kunz, H. Rui, A. Biswas and R. Adelung, *Adv. Mater.*, 2006, **18**, 1059.

47 M. Lang, L. He, F. Xiu, X. Yu, J. Tang, Y. Wang, X. Kou, W. Jiang, A. V. Fedorov and K. L. Wang, *ACS Nano*, 2012, **6**, 295.

48 Z. Sun, S. Liufu, X. Chen and L. Chen, *CrystEngComm*, 2010, **12**, 2672.

49 P. Larson, V. A. Greanya, W. C. Tonjes, R. Liu, S. D. Mahanti and C. G. Olson, *Phys. Rev. B: Condens. Matter*, 2002, **65**, 085108.

50 Z. Ren, A. A. Taskin, S. Sasaki, K. Segawa and Y. Ando, *Phys. Rev. B: Condens. Matter*, 2011, **84**, 165311.

51 Y. Pan, D. Wu, J. R. Angevaare, H. Luigjes, E. Frantzeskakis, N. de Jong, E. van Heumen, T. V. Bay, B. Zwartsenberg, Y. K. Huang, M. Snelder, A. Brinkman, M. S. Golden and A. de Visser, *New J. Phys.*, 2014, **16**, 123035.

52 L. Galletti, S. Charpentier, P. Lucignano, D. Massarotti, R. Arpaia, F. Tafuri, T. Bauch, Y. Suzuki, A. Tagliacozzo, K. Kadowaki and F. Lombardi, *Physica C*, 2014, **503**, 162.

53 H. Tang, D. Liang, R. L. J. Qiu and X. P. A. Gao, *ACS Nano*, 2011, **5**, 7510.

54 J. G. Analytis, J.-H. Chu, Y. Chen, F. Corredor, R. D. McDonald, Z. X. Shen and I. R. Fisher, *Phys. Rev. B: Condens. Matter*, 2010, **81**, 205407.

55 R. Kilaas, *J. Microscopy*, 1998, **190**, 45.

56 P. A. Stadelmann, *Ultramicroscopy*, 1987, **21**, 131.